Ocean Dynamics (2013) 63:923–941
DOI 10.1007/s10236-013-0633-1

Seasonality of the submesoscale dynamics in the Gulf Stream region

**Jean Alberto Mensa · Zulema Garraffo ·
Annalisa Griffa · Tamay Mehmet Özgökmen ·
Angelique Haza · Milena Veneziani**

Received: 8 March 2013 / Accepted: 3 June 2013 / Published online: 5 July 2013

Abstract Frontogenesis and frontal instabilities in the mixed layer are known to be important processes in the formation of submesoscale features. We study the seasonality of such processes in the Gulf Stream (GS) region. To approach this problem, a realistic simulation with the Hybrid Coordinate Ocean Model is integrated for 18 months at two horizontal resolutions: a high-resolution ($1/48°$) simulation able to resolve part of the submesoscale regime and the full range of mesoscale dynamics, and a coarser resolution ($1/12°$) case, in which submesoscales are not resolved. Results provide an insight into submesoscale dynamics in the complex GS region. A clear seasonal cycle is observed, with submesoscale features mostly present during winter. The submesoscale field is quantitatively characterized in terms of deviation from geostrophy and 2D dynamics. The limiting and controlling factor in the occurrence of submesoscales appears to be the depth of the mixed layer, which controls the reservoir of available potential energy available at the mesoscale fronts that are present most of the year. Atmospheric forcings are the main energy source behind submesoscale formation, but mostly indirectly through mixed layer deepening. The mixed layer instability scaling suggested in the (Fox-Kemper et al., J Phys Oceanogr 38:1145–1165, 2008) parametrization appears to hold, indicating that the parametrization is appropriate even in this complex and mesoscale dominated area.

Keywords Submesoscale · Seasonality · Frontogenesis · Mixed layer instabilities · Ageostrophic dynamics · Gulf Stream · HYCOM · Multi-scale

1 Introduction

Ocean dynamics developing at the planetary scale is dominated by Earth's rotation and density stratification. Motion of water masses at these scales is governed by the balance between Coriolis force and pressure gradient. In this regime, planetary rotation dominates over advection, and the Rossby number is small, $Ro = U/fL \ll 1$ (U and L are the characteristic scales for horizontal velocity and length, and f is the Coriolis parameter). At these scales, the energy injected by the atmosphere is released through baroclinic instabilities in form of kinetic energy (McWilliams 2008; Molemaker et al. 2010), and dissipation is provided by friction within the boundary layers.

At the small scales, on the other hand, the effect of planetary rotation is negligible ($Ro \gg 1$), and flows have the characteristics of the extensively studied non-rotating regime: flows are fully three-dimensional, and the equations of motion are dominated by advection and diffusion separated by the inertial range (Kolmogorov 1941). Turbulence in this regime is fully three-dimensional and charac-

Responsible Editor: John Wilkin

J. A. Mensa (✉) · A. Griffa · T. M. Özgökmen · A. Haza
RSMAS, University of Miami, 4600 Rickenbacker Csw,
Miami, FL 33149-1098, USA
e-mail: jmensa@rsmas.miami.edu

Z. Garraffo
IMSG at NOAA/EMC, NCWCP,
5830 University Research Court, College Park, MD 20740, USA

A. Griffa
ISMAR/CNR, U.O.S di Pozzuolo di Lerici (SP),
Forte Santa Teresa, 10932 Lerici, La Spezia, Italy

M. Veneziani
Division T-3 MSB216, Fluid Dynamics and Solid Mechanics,
Los Alamos National Laboratory,
Los Alamos, NM 87545, USA

terized by a forward cascade of energy allowing viscous dissipation.

These two regimes are separated by a broad range of scales, ranging from $\mathcal{O}(100)$ m to $\mathcal{O}(10)$ km (Thomas et al. 2008), usually called "submesoscale" (here on, SM). These scales are characterized by a weakening of the geostrophic constrains and a transition towards isotropic turbulence (Molemaker et al. 2005, 2010; Muller et al. 2005; McWilliams 2008; Molemaker et al. 2010).

SM dynamics have been extensively studied for the past few decades through models and theoretical studies (McWilliams 1985b), but real ocean observations are still rare (Flament et al. 1985; Pollard and Regier 1992; Ferrari and Rudnick 2000; D'Asaro et al. 2011). An important evidence of such regime comes from the study on the productivity levels in the mixed layer. Productivity is sustained by fluxes of nutrients from below the photic zone that can be provided by near-coast upwelling or baroclinic instabilities in regions far from the boundaries. In these regions, the observed productivity due to mesoscale eddies has been found (McGillicuddy Jr. et al. 2003, 2007) to account for only 20–30 % of the annual amount of nutrients, and the observed spatial scale of surface nutrients is too fine for being produced by mesoscale dynamics, thereby suggesting the presence of a SM regime. Klein and Lapeyre (2009) reviewed recent developments in this direction showing that submesoscale dynamics could indeed account for the high productivity observed near the surface.

Lagrangian drifters are another tool that has been successfully employed to study SM features. In the past few years, dedicated experiments with multiple drifter launchings (Koszalka et al. 2009; Lumpkin and Elipot 2010; Schroeder et al. 2011) have been carried out in order to characterize the SM regime. In particular, some studies indicate that submesoscale features play an active role in Lagrangian dispersion (Lumpkin and Elipot 2010; Schroeder et al. 2012), while others suggest that most of the transport is dominated by large and mesoscale features (Koszalka et al. 2009; Schroeder et al. 2011).

The uncertainty coming from real ocean observations underlines the importance of understanding the mechanisms determining the presence of SM features. In the past years, high-resolution numerical simulations greatly enhanced our understanding on the mechanisms behind the formation of SM features with studies in idealized or semi-idealized configurations (Mahadevan and Tandon 2006; Mahadevan 2006; Boccaletti et al. 2007; Thomas and Ferrari 2008; Thomas et al. 2008; Molemaker et al. 2010; Özgökmen et al. 2011, 2012; Özgökmen and Fischer 2012). Realistic simulations of these processes are also needed.

Basin-wide simulations have been successfully implemented to study areas with strong SM activity such as upwelling regions (Capet et al. 2008b, c, d) and continental shelves (Capet et al. 2008a) and confirmed that SM features are affected by the characteristics of the mixed layer and the strength of the horizontal density gradients (Fox-Kemper et al. 2008; Lévy et al. 2011; Badin et al. 2011).

The present work aims to contribute to the understanding on the mechanisms responsible for the presence of SM features in the mixed layer, considering a realistic high-resolution model of the recirculating region of the Gulf Stream (here on, GS). This region is of primary importance for ecological and climate-related problems and has been intensively studied in the literature in terms of mesoscale dynamics, ring formation, and transport (Auer 1987; Clarke et al. 1980; Johns et al. 1995; Sato and Rossby 1995; Hogg 1992), but its submesoscale dynamics have not been explored yet. This work provides an analysis of the SM field in this area in terms of generation mechanisms, statistical properties, and dependence on environmental parameters and seasonality.

The study is carried out using Hybrid Coordinate Ocean Model (HYCOM) which has been extensively and successfully tested in this region (Halliwell 2004; Chassignet et al. 2003, 2009; Smith et al. 2000).

The model is integrated for 18 months in a realistic configuration at two horizontal resolutions: a high-resolution simulation (HR) $1/48°$ horizontal resolution ($\sim$ 2 km) that is partially SM resolving, and a low-resolution simulation (LR) at $1/12°$ horizontal resolution ($\sim$ 8 km) that does not explicitly resolve the submesoscale dynamics, but resolves mesoscale features. Analysis of the high-resolution simulation and comparison between the two simulations allow us to isolate processes that are directly linked to submesoscale. Details of the model configuration are described in Section 2. Results are presented in Sections 3, 4, and 5. In Section 3, a review of the processes responsible for the formation of SM features is presented; in Section 4, the characteristics of the generated SM features are investigated; and in Section 5, the connection between seasonality of the mixed layer and the generation of SM features is described.

2 Model setup

2.1 Model configuration

The HYCOM (Bleck 2002; Halliwell 2004; Chassignet et al. 2006) is used to simulate the Gulf Stream at two different resolutions. The HR simulation is done in a Mercator horizontal grid at $1/48°$ grid size and has 30 vertical hybrid (z-sigma-isopycnal) layers, of which the top six layers are allowed to be in z coordinates, and the ocean interior is generally in potential density coordinates, referred to 20 MPa, σ_2 (the equation of state is written in σ_2 with thermobaricity). The lateral boundary conditions are of a one-way nesting, with the external solution coming from a coarser resolution (1/12°) simulation (LR) covering the Atlantic Ocean and the Mediterranean Sea in the latitudinal range between 28°S and 80°N (Fig. 1, Chang et al. 2009). The lateral boundary conditions for the LR simulation are closed but with relaxation to climatology, for the thermodynamic variables, in the northern and southern boundaries.

The nested simulation (HR) covers the region from 81.44°W 28.78°N to 50°W 45.72°N. It is initialized from the low-resolution solution on January 1 after 8 years of spin-up and ends at day 135 of the following year (May 15), spanning a total of 501 days. A period of approximately 1 month is needed for the HR simulation to adjust from the LR simulation. In order to avoid the possible influence of the spin-up, we will focus on one model year in the following, going from May 15 (day 135 from initialization) through the end of the simulation. In the paper, we show typical snapshots of winter (February 1) and summer season (July 19).

The one-way nesting method employed here is available in the standard HYCOM source. For the barotropic flow, boundary conditions following the method of characteristics are applied to the normal velocities and pressure, while parallel velocities are imposed. For the baroclinic flow, normal velocities and total mass fluxes are prescribed, while tangential velocities are nudged at the boundary; interface pressures are nudged within a finite width zone.

An example of the HR simulation is shown in Fig. 2 where a snapshot of sea surface temperature (SST) is displayed for the winter season. The configuration of the HR simulation has been used by Haza et al. (2012) to study the Lagrangian properties of the Gulf Stream. The model near-surface circulation shows a defined Gulf Stream extension, Gulf Stream velocities, and eddy kinetic energy consistent in magnitude and location of the current with drifter data analysis (Fratantoni 2001; Garraffo et al. 2001; Lumpkin and Johnson 2013). The model sea surface height variability (not shown) is 20–40 cm in the Gulf Stream extension, consistent with altimeter data analysis (Ducet et al. 2000).

The present study focuses on a portion of the recirculation zone of the GS, region A (from 72.02°W 30.162°N to 55.86°W 33.442°N), characterized by the recirculating part of the subtropical gyre. This region is chosen because it allows us to study the dynamics of SM features in the presence of strong mesoscale features such as those generated in proximity of the GS. In order to visualize SM features, diagnostics are also computed for a smaller region (region S) located inside region A. Diagnostics are obtained at different depths after interpolation of the original hybrid vertical grid to a fixed depth grid.

The LR and HR simulations are based on the same depth data set, parameters, and forcing. The model topography was obtained from the Digital Bathymetric Data Base. The thermodynamic atmospheric forcing is based on monthly values from the ECMWF 40-year reanalysis (ERA40, Uppala et al. 2005) for years 1978–2002. The mechanical forcing is based on the same data set plus 6-hourly perpetual year wind stress and wind speed anomalies (derived from Navy Operational Global Atmospheric Prediction System Model, for January 2003–January 2004). Atmospheric forcing values are extrapolated from the ocean onto land to avoid discrepancies between atmospheric and

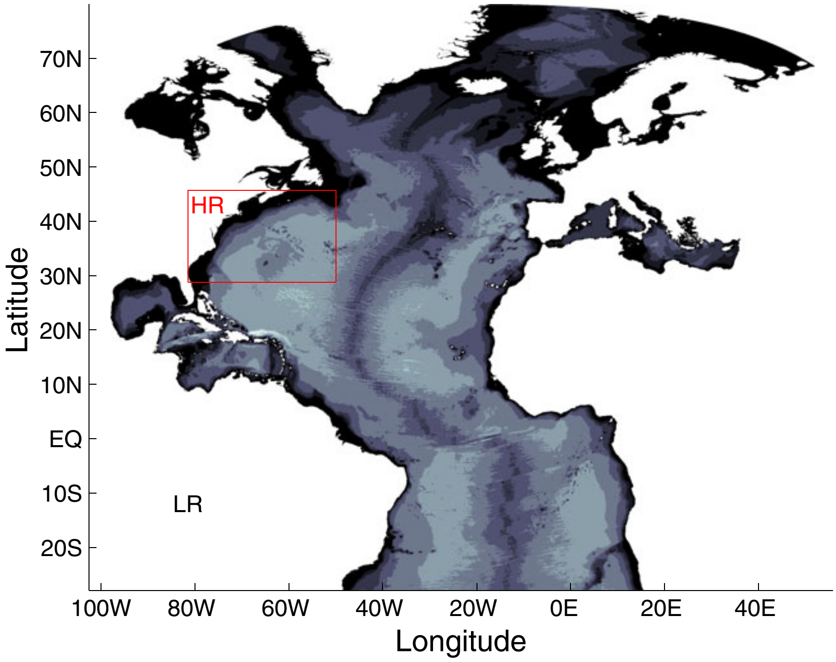

Fig. 1 The domain of the *LR* simulation of the Atlantic Ocean at 1/12° horizontal resolution, where the *box* represents the extent of the nested *HR* simulation at 1/48° horizontal resolution. The *gray color* represents the bathymetry of the region

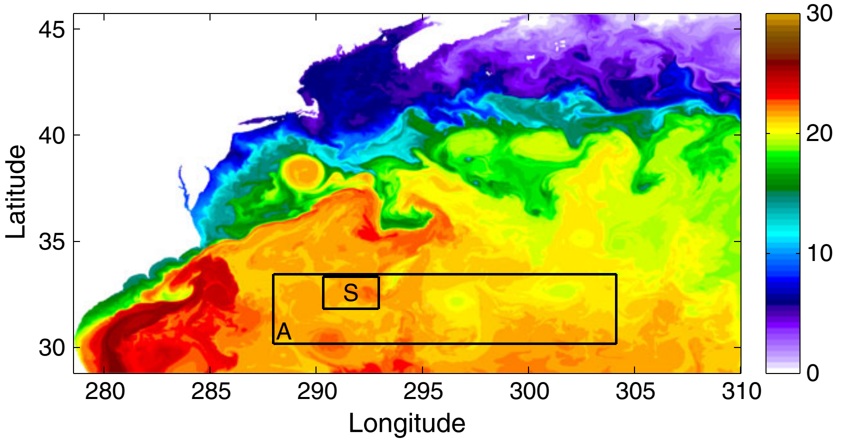

Fig. 2 SST (in degrees Celsius) snapshot during the winter season from the HR simulation. The *boxes* represent the regions over which diagnostics are computed

ocean model land–sea masks (Kara et al. 2007), and several bias corrections are applied that are in use at the Naval Research Laboratory, some of them described for the ERA40 simulation by Metzger et al. (2010) (wind speed corrected through correlations with satellite observations (Wallcraft et al. 2009), limiting maximum wind velocity to non-hurricane winds).

The vertical mixing scheme is based on the KPP parametrization of Large et al. (1994). Horizontal mixing is parametrized as a linear combination of Laplacian and biharmonic mixing scaled with the grid size (Chassignet and Garraffo 2001).

2.2 Flow decomposition

For a number of diagnostics presented in the following, it is useful to separate the mesoscale and large fraction from the SM fraction of the flow field. This is done by filtering in space the variables of interest and removing the filtered fraction from the total field to obtain the SM residuals. The filter used here is a one lobe sine function with equation $f(x) = \sin(x\cdot 2\pi/\lambda)/(x\cdot 2\pi/\lambda)\cdot\sin\left(x \cdot 4\pi/\lambda^2\right) / \left(x \cdot 4\pi/\lambda^2\right)$, where the parameter λ is selected by minimizing the difference between the filtered fields in the mixed layer, where SM features are expected to be abundant (60-m depths, winter HR), and the same unfiltered fields below the mixed layer (500 m), and where SM features are expected to be absent in the first approximation. The fields considered are the two components of horizontal velocity u and v and density ρ.

In Fig. 3, the RMS difference between each filtered variable at a 60-m depth ($V_F(\lambda)_{60\text{ m}}$) and the original field at 500 m ($V_{O\,500\text{ m}}$) is computed as function of λ,

$$D = \sqrt{(V_F(\lambda)_{60\text{ m}} - V_{O\,500\text{ m}})^2}. \tag{1}$$

where D is normalized between 0 and 1 to facilitate the comparison. Results for the two velocity components are similar, showing a minimum around $\lambda \approx 100$ km, while for density, the minimum is around $\lambda \approx 50$ km. In the following, we choose a reference value of $\lambda = 70$ km for filtering. Obviously, the partition between mesoscale and SM is not expected to be perfect, given the complexity of the flow and its multiscale nature. For this reason, in the following, we also perform additional sensitivity tests for selected diagnostics. Notice that $\lambda = 70$ km approximately corresponds to filtering scales smaller than the first baroclinic Rossby deformation radius, which is expected to be of the order of 30 km in this area (Chelton et al. 2010).

As an example, results of the filtering with $\lambda = 70$ km are shown in Fig. 4 for speed $\left(c = |\mathbf{u}| = \sqrt{u^2 + v^2}\right)$ over the whole domain, where filtered quantities and anomalies are displayed next to the original field (Fig. 4a). Here and in the following, the mesoscale fraction is represented by the over-bar, while submesoscale anomalies, by the prime ($c = \bar{c} + c'$). The mesoscale field appears well resolved (Fig. 4b), and SM features (Fig. 4c) are ubiquitous in the winter

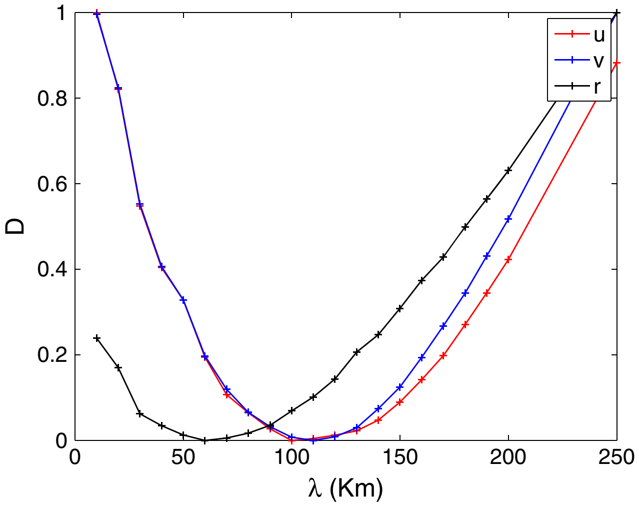

Fig. 3 Values of D (1) for u, v, and density ρ as function of λ computed over region A during the winter season of the all domain of the HR simulation

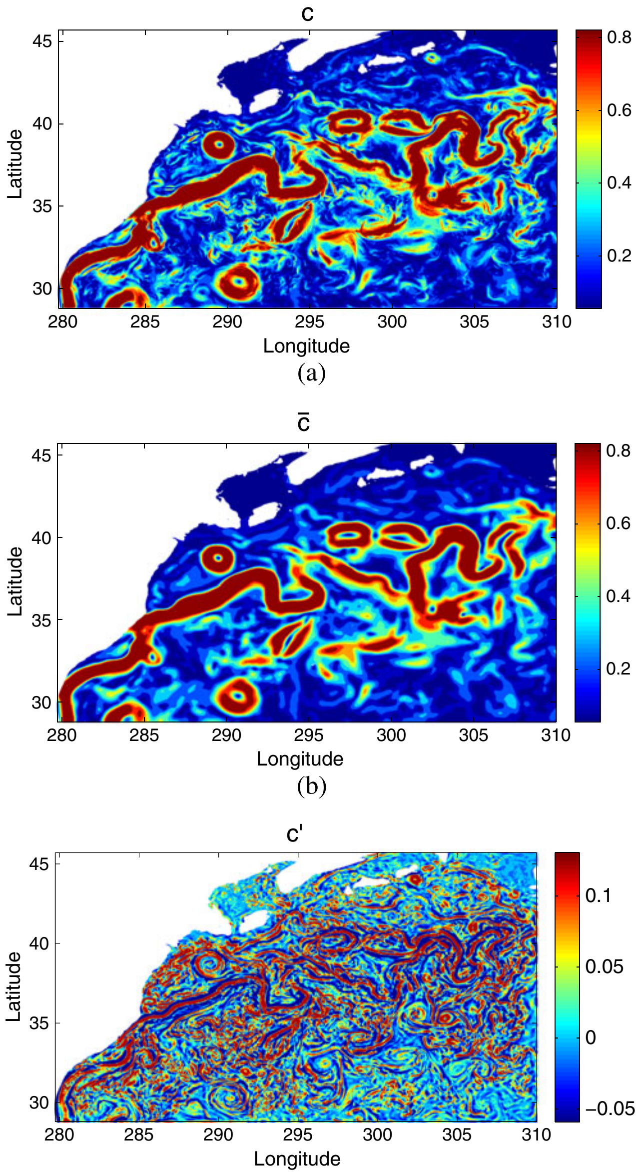

(a)

(b)

(c)

Fig. 4 **a** Total (c), (**b**) filtered ($\bar{c}$), and (**c**) residual speed (c', in meter per second) at a 60-m depth during winter season for the HR simulation

mixed layer. SM features are especially developed around the edges of mesoscale structures such as rings, eddies, and jets, as can be expected in a strain-dominated region such as the GS (Bishop 1993; McWilliams et al. 2009a, b).

3 Mechanisms of submesoscale generation: frontogenesis and mixed layer instabilities

The SM regime is characterized by the ability to transfer energy from available potential energy (APE) and kinetic energy (KE) of the mesoscale to smaller scales, opening the road toward the dissipative scales (McWilliams 2008; Molemaker et al. 2010). In particular, APE, stored in the highly energetic mesoscale features of the Gulf Stream, can be transferred to the smaller scales by *frontogenesis* (Hoskins 1982; Pedlosky 1987; Giordani and Caniaux 2001; Thomas and Lee 2005; Lapeyre et al. 2006) and then released in the form of eddy kinetic energy (EKE) by *mixed layer instabilities* (MLI) (Stone 1966, 1970; Boccaletti et al. 2007).

Here, we investigate the mechanisms of frontogenesis and MLI in the GS simulations, considering first specific examples occurring in winter and summer snapshots and then quantifying their overall time dependence in terms of integral quantities.

3.1 Frontogenesis in the mixed layer

Frontogenesis develops mostly near the ocean surface, where the absence of vertical velocities allows straining from mesoscale eddies to increase density variance, therefore leading to a very effective sharpening of existing density fronts (Bishop 1993; Lapeyre et al. 2006; McWilliams et al. 2009a, b). Surface horizontal density gradients $\nabla_h \rho$ are in thermal wind balance with a surface jet that generates, as byproduct of frontal intensification, increased vorticity at the flanks of the front and regions with strong horizontal strain.

Frontogenesis is commonly studied in terms of frontal tendency function F (Hoskins and Bretherton 1972; Capet et al. 2008c),

$$F = \frac{D|\nabla_h \rho|^2}{Dt} = \mathbf{Q} \cdot \nabla_h \rho, \qquad (2)$$

where ρ is density, $\mathbf{Q}$ is the Q-vector defined in Eq. 3 and $\nabla_h = \partial/\partial x\,\hat{\mathbf{i}} + \partial/\partial y\,\hat{\mathbf{j}}$. A positive sign of F represents an increase in time of the magnitude of the density gradient indicating *frontogenesis*, while a negative sign indicates *frontolisis*.

The Q-vector (Hoskins 1982),

$$\mathbf{Q} = (Q_1, Q_2) = \left(-\frac{\partial \mathbf{u}}{\partial x} \cdot \nabla_h \rho,\ -\frac{\partial \mathbf{u}}{\partial y} \cdot \nabla_h \rho\right), \qquad (3)$$

computed with the full horizontal velocities (geostrophic and ageostrophic), affects the evolution of the thermal wind components disrupting the thermal wind balance. The thermal wind balance is then compensated by a secondary ageostrophic circulation across the front. The resulting cross-front circulation is described by the Ω-equation which expresses the spatial distribution of the vertical quasi-geostrophic velocity, ω, as a function of the horizontal divergence of $\mathbf{Q}$ (Hoskins et al. 1978; Giordani and Planton 2000; Giordani and Caniaux 2001),

$$N^2\nabla_h^2\omega + f_0^2\frac{\partial^2\omega}{\partial z^2} = -2\frac{g}{\rho_0}\nabla_h\cdot\mathbf{Q}, \tag{4}$$

where N^2 is the Brunt–Väisälä frequency, $N^2 = b_z$ (subscript represents the partial derivative with respect to z), with b as the buoyancy $b = -g\rho/\rho_0$, and ρ_0 as the reference density computed as the average density in the mixed layer of region A.

Examples of vertical recirculations indicative of frontogenetic activity during winter in subregion S are shown in terms of ω for HR Fig. 5a. Alternate bands of vertical velocity are evident along the fronts, spatially correlated to regions with large values of F (not shown). Notice that ω is computed by inverting the Ω-equation, and therefore, strictly speaking, represents only the QG component of the frontal vertical velocity (Mahadevan and Tandon 2006). Typical values of ω, though, have a magnitude on the order of 15 m per day that accounts for most of the vertical velocity computed by HYCOM as divergence of the horizontal velocity field. These values compare well with observations (Pollard and Regier 1992).

During summer, the frontal vertical recirculations appear significantly weaker, as shown by the snapshot in Fig. 5b. Values of ω are almost one order of magnitude smaller across the fronts with respect to the winter season, and the patterns do not show the typical bands of alternated positive and negative values at the flanks of the density fronts.

The ω vertical velocity has also been computed for the LR simulation in winter (Fig. 5c). Fronts appear significantly weaker in intensity (about 30 % less), and they occur mainly at the mesoscale, confirming that the structures in Fig. 5a emerge at increased resolution, and they are linked to submesoscale.

The frontal vertical velocity can be quantified by computing the average value of $|\omega|$ over region A and can be regarded as a proxy for frontal intensity. The time series of the average $|\omega|$ at 5 m is shown in Fig. 6, indicating a clear seasonal cycle with maximum values during winter (around February) and minimum values in summer (around August).

3.2 Mixed layer instabilities

Once fronts intensify, instabilities of various types can occur (Haine and Marshall 1998). Here, we consider the general class of baroclinic MLI (Boccaletti et al. 2007; Stone 1966, 1970), and we propose to diagnose them through their net effect, i.e., the conversion rate of APE to eddy kinetic energy EKE (Boccaletti et al. 2007; Fox-Kemper et al. 2008; Capet et al. 2008c).

The conversion of APE in EKE is common to all baroclinic instabilities; therefore, to ensure that only the submesoscale fraction is considered, quantities are filtered as described in Section 2.2. The release of APE can be quantified in terms of eddy vertical buoyancy flux $w'b'$ (where primes denote the SM residual) which is expected to show

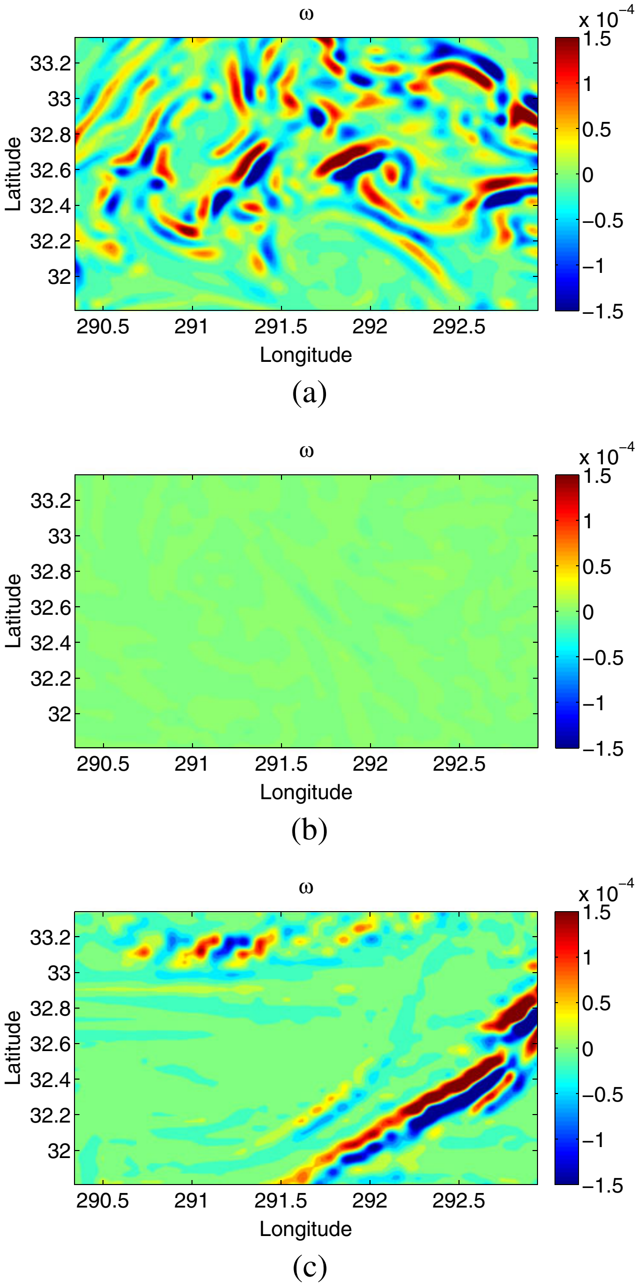

(a)

(b)

(c)

Fig. 5 Vertical velocity ω (in meter per second) computed for HR **a** during winter at a 60-m depth and **b** during summer at a 5-m depth, and **c** for LR during winter at a 60-m depth. Depths are chosen in order to represent the mixed layer

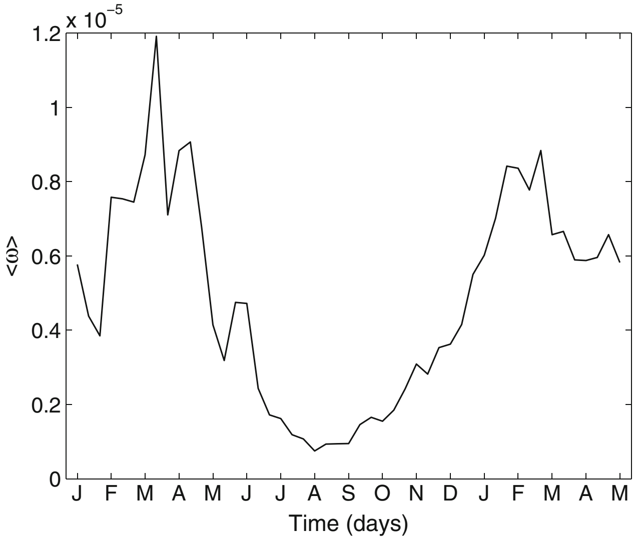

Fig. 6 Time series of the modulus of vertical velocity $|\omega|$ (in meter per second) computed as average values over region A at a 4-m depth for the HR simulation

positive and negative values at the flanks of the front as the secondary ageostrophic circulation drives the density anomalies.

Computing $w'b'$ for subregion S (Fig. 7) shows that, indeed, positive and negative values are present at the two sides of the front. Overall larger values are found in the winter season (Fig. 7a) compared to summer (Fig. 7b) as expected due to the stronger vertical velocities found during winter that drive large buoyancy fluxes. For LR (Fig. 7c), values are comparable in magnitude to HR, but only few relatively large features remain after filtering.

In Fig. 8, a typical winter profile of $w'b'$ averaged over region A is shown. Average flux is always positive, with zero value at the surface (consistently with the boundary condition $w = 0$) and small values below 300 m, as expected given that the MLI activity is confined in the mixed layer. A clear maximum can be seen at approximately 80 m, indicating the presence of a buoyancy flux vertical divergence, with negative vertical flux gradients contributing to a positive buoyancy tendency in the upper 80 m and positive gradients below. The tendency towards a lighter upper mixed layer and heavier lower mixed layer contributes to a net restratification effect. The pattern is consistent with results from idealized MLI numerical models (Boccaletti et al. 2007; Fox-Kemper and Ferrari 2008) as well as with realistic models in the California Current and Argentinean shelf (Capet et al. 2008a), and it indicates that also in the GS region, heavily influenced by strong mesoscale and rings, the mixed layer dynamics is largely controlled by MLIs.

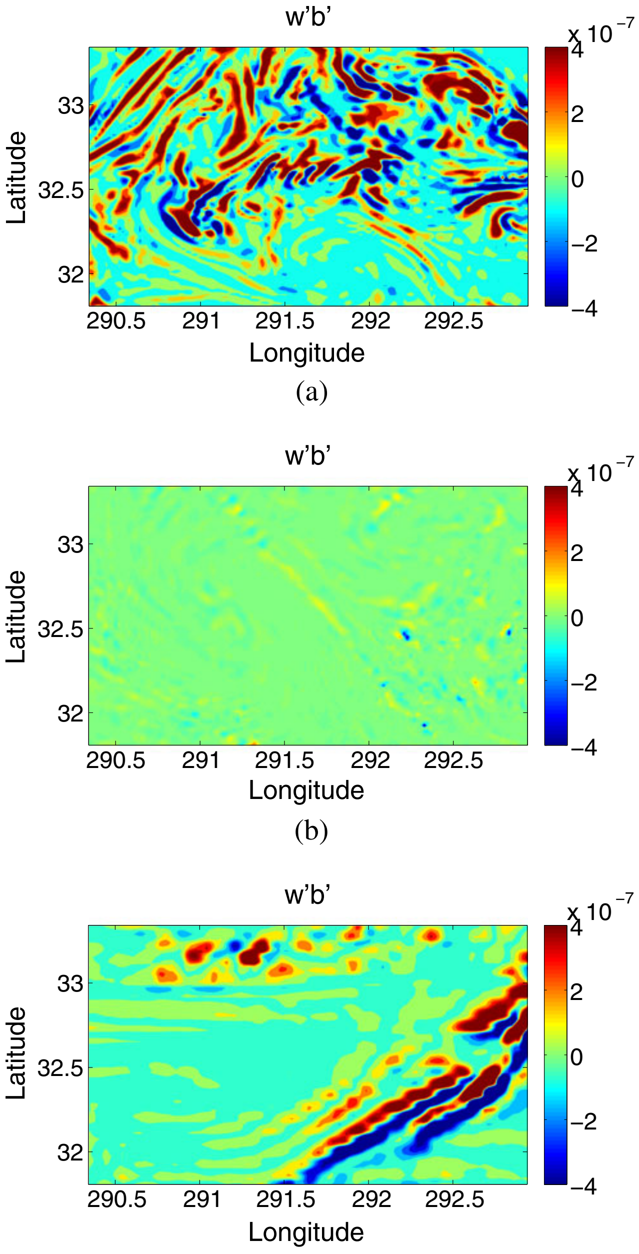

(a)

(b)

(c)

Fig. 7 $w'b'$ (in square meter per cubic second) for **a** winter at 60 m, **b** summer season at 5 m in HR, and **c** for winter LR at 60 m

In order to quantify the net release of APE, we integrate over the mixed layer depth (MLD) the average of $w'b'$ over region A, obtaining the rate of conversion of APE in EKE, PK (Boccaletti et al. 2007; Fox-Kemper et al. 2008; Capet et al. 2008c),

$$\mathrm{PK} = \frac{1}{\mathrm{MLD}} \int_0^{-\mathrm{MLD}} \left\langle w'b' \right\rangle_{xy} dz. \tag{5}$$

where the angle brackets ($\langle . \rangle_{xy}$) represent the averaging over region A. MLD is computed by HYCOM as the depth at which the density difference with respect to the surface is equivalent to a 0.3 °C temperature change (leaving salinity constant).

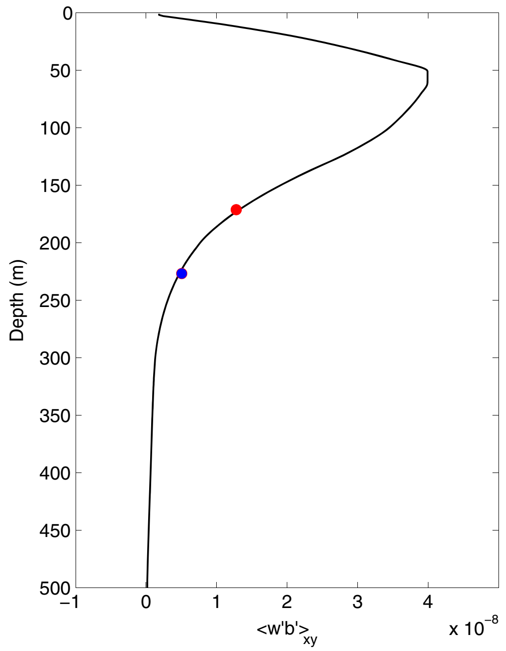

Fig. 8 Vertical dependence of $w'b'$ (in square meter per cubic second, Eq. 5) averaged over region A for HR during winter season. The *dots* represent the mixed layer depth (and corresponding value of PK) for HR ($\sim$ 71 m, *red dot*) and LR ($\sim$ 226 m, *blue dot*)

The value of PK corresponding to the snapshots in Fig. 7 in winter and summer for the HR simulation are $2.86 \cdot 10^{-8}$ and $1.25 \cdot 10^{-9}$ m^{2}s^{-3}, respectively, showing that values are overall larger during winter than during summer. Also, values are typically larger on average in the HR simulation as features developing in LR are suppressed by the filtering. In Fig. 9, the complete time series of $\langle w'b' \rangle_{xy}$ is computed, showing a clear seasonal cycle in phase with the seasonality of the vertical velocity ω. Sensitivity of the time series to different filtering length scales was tested using values of $\lambda = 40$ km and $\lambda = 130$ km. Results show a seasonal cycle with values of the same order of magnitude of the current filter at 70 km, but with smaller or larger values of PK for smaller and larger values of λ. The time series for LR shows that a seasonal cycle in PK exists despite the filtering, meaning that a scale separation is not fully captured by the filtering or not present.

4 Diagnosing the characteristics of submesoscale features

Here, we quantitatively describe the characteristics of the flow in the mixed layer with specific interest in the occurrence of submesoscale features which we expect to be particularly prominent in winter when the mechanisms of frontogenesis and MLI are more active. SM features are expected to be characterized by scales of the order of the mixed layer Rossby radius of deformation, with significant deviation from geostrophy and high relative vorticity and Rossby number (Thomas et al. 2008). Various diagnostics are presented here to quantify the seasonality of SM.

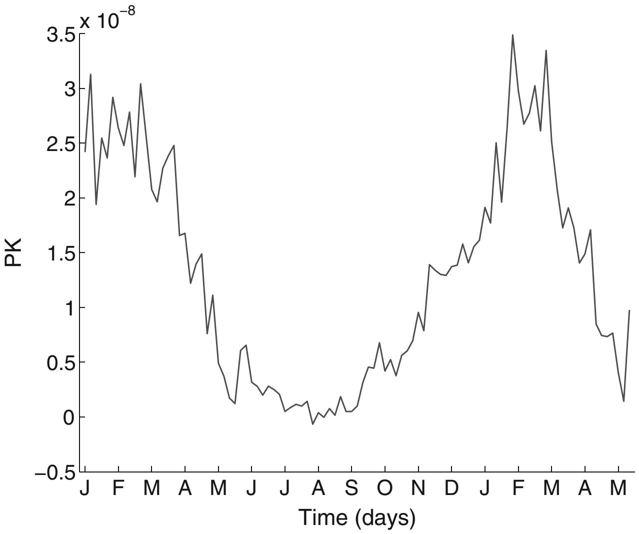

Fig. 9 Time series of the conversion rate of available potential energy into eddy kinetic energy, PK (in square meter per cubic second), as computed in Eq. 5. PK is integrated over region A at a 5-m depth for HR

4.1 Horizontal length scale

A way to quantify the scale of the features developing in the flow field is by computing the spectra of kinetic energy. From these, it is then possible to quantify the seasonality of the energy associated to the SM regime integrating, for each day, the kinetic energy spectrum over the SM wave numbers,

$$\mathrm{KE}_s(t) = \int_{R_{\mathrm{SM}}{}^{-1}}^{2\Delta x^{-1}} \mathrm{KE}(k, t)dk, \tag{6}$$

where $\mathrm{KE}_s(t)$ is the portion of the total kinetic energy associated to the submesoscale regime, i.e., the fraction of KE_s integrated over wave numbers from $R_{\mathrm{SM}}{}^{-1}$, where R_{SM} is the length scale of the submesoscale dynamics, to $2\Delta x^{-1}$, where Δx is the grid size. R_{SM} is a function of the Rossby deformation radius for the mixed layer, Rd_{ML} (Özgökmen et al. 2011),

$$Rd_{\mathrm{ML}} = \frac{\sqrt{\mathrm{MLD}\, g\, \Delta\rho/\rho_0}}{f}, \tag{7}$$

where ρ_0 is the vertical average density across the mixed layer, and $\Delta\rho$ is the density jump across the mixed layer. In the following, we considered a value of $R_{\mathrm{SM}} = 5\, Rd_{\mathrm{ML}}$ as it has been suggested by Eldevik (2002).

Equation 6 has been estimated for both resolutions (Fig. 10), showing a clear seasonal cycle with larger values of KE associated to SM features in HR, as expected from the fact that the HR simulation resolves more small scale features and thus covers a broader range of wave numbers than LR.

4.2 Deviation from gradient wind balance

A measure of how SM features are effectively unbalanced comes from the quantification of the deviation from gradient wind balance (McWilliams 1985a; Capet et al. 2008c; Molemaker et al. 2010),

$$\epsilon(\mathbf{x}, t) = \frac{\left| -\nabla_{\mathbf{h}} \cdot (\mathbf{u} \cdot \nabla_{\mathbf{h}} \mathbf{u}) + f\zeta - \frac{1}{\rho}\nabla_h^2 p \right|}{|\nabla_{\mathbf{h}} \cdot (\mathbf{u} \cdot \nabla_{\mathbf{h}} \mathbf{u})| + f|\zeta| + \left| \frac{1}{\rho}\nabla_h^2 p \right| + \mu}, \qquad (8)$$

where ζ is the vertical component of the relative vorticity, and velocities and derivatives are only horizontal ($\mathbf{u} = (u, v)$). The term $\mu = f\zeta_{\mathrm{RMS}} + \rho^{-1}\left(\nabla_h^2 p\right)_{\mathrm{RMS}}$, where RMS indicates root mean square values, is added to the denominator to avoid situations dominated by the Coriolis force from being identified as unbalanced. $\epsilon(\mathbf{x}, t)$ can vary between 0, for completely *balanced flows*, and 1, for completely *unbalanced dynamics*. Snapshots of this diagnostic in the mixed layer for winter and summer in HR are shown for a subregion of region A in Fig. 11, indicating that deviations occur in both seasons but with different characteristics. In winter, the deviations are mostly in filaments and fronts, suggesting the presence of SM, while in summer, they occur only in few regions near the large mesoscale structures.

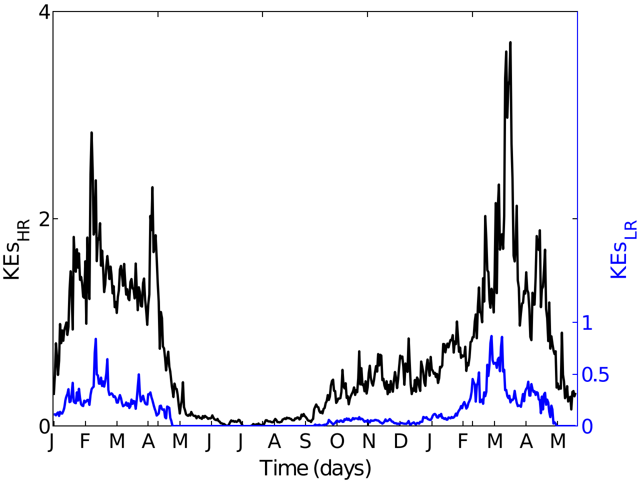

Fig. 10 Kinetic energy (in square meter per square second) integrated over the submesoscale wave numbers computed from Eq. 6, for both HR (*black line*) and LR (*blue line*)

4.3 Relative vorticity and Rossby number

SM features are expected to be significantly ageostrophic and characterized by high relative vorticity. A quantitative view of the seasonal and resolution-dependent distribution of relative vorticity normalized by planetary vorticity, i.e., the Rossby number $Ro = |\zeta/f|$, can be observed in Fig. 12. In Fig. 12a, Ro is spatially averaged over region A and computed as a function of depth for each resolution and season. Ro shows a clear intensification in the mixed layer, especially evident during winter in HR. This is consistent with a signature of the intensification of submesoscale features. The seasonal variations of Ro are also evident in Fig. 12b where the frequency of instances of $Ro > 0.5$ over region A has been computed throughout the year for the 5- and 500-m depth at both resolutions. Figure 12a, b shows that most of the ageostrophic values of ζ occur in the mixed layer, mostly in HR, with a maximum during the winter season.

More details on the distribution of ζ, including its sign, are shown by the probability density functions (PDFs) of ζ/f_0 (Fig. 13). The difference between LR and HR, which is expected to be due to the emergence of submesoscale, is evident especially in the mixed layer and is characterized by enhanced deviation from a Gaussian distribution and

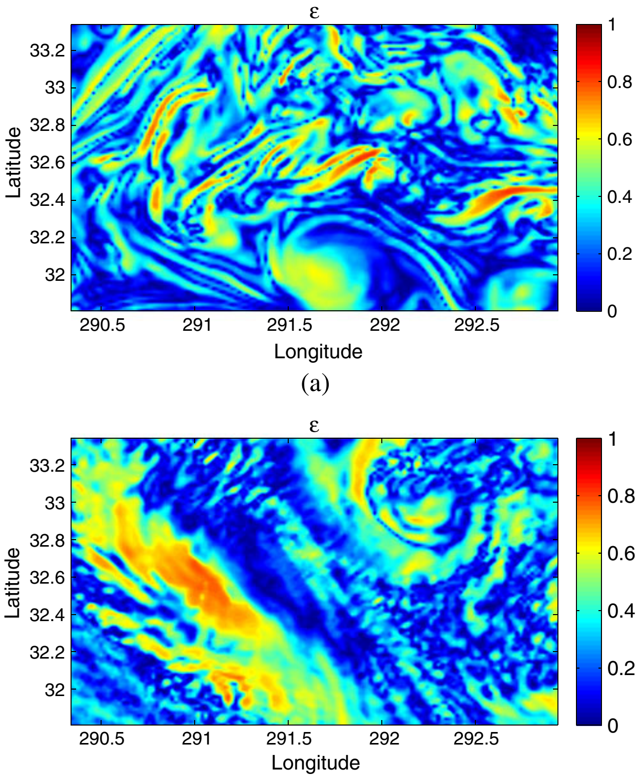

(a)

(b)

Fig. 11 Unbalanced regions computed in region S for **a** winter at a 60-m depth and **b** summer season at a 5-m depth

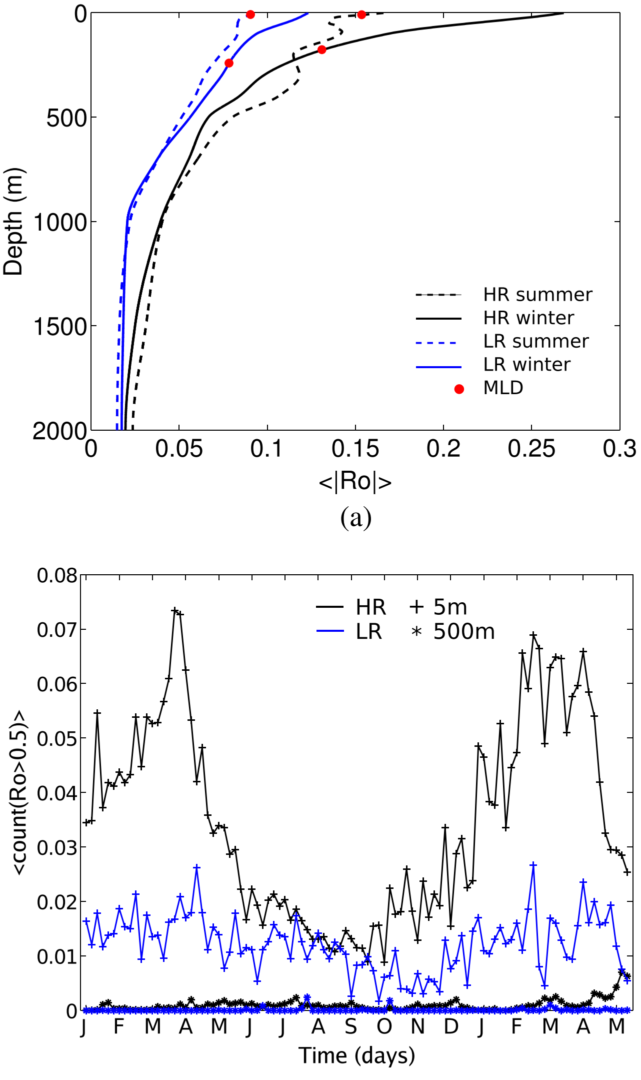

(a)

(b)

Fig. 12 **a** Vertical dependence of the Rossby number averaged over region A for summer (*dashed lines*), winter (*solid lines*), HR (*black lines*), and LR (*blue lines*). The *red dots on the curves* represent the mixed layer depth. **b** Seasonal trend of the frequency of instances of $Ro > 0.5$ over region A for both resolutions at 5- and 500-m depth

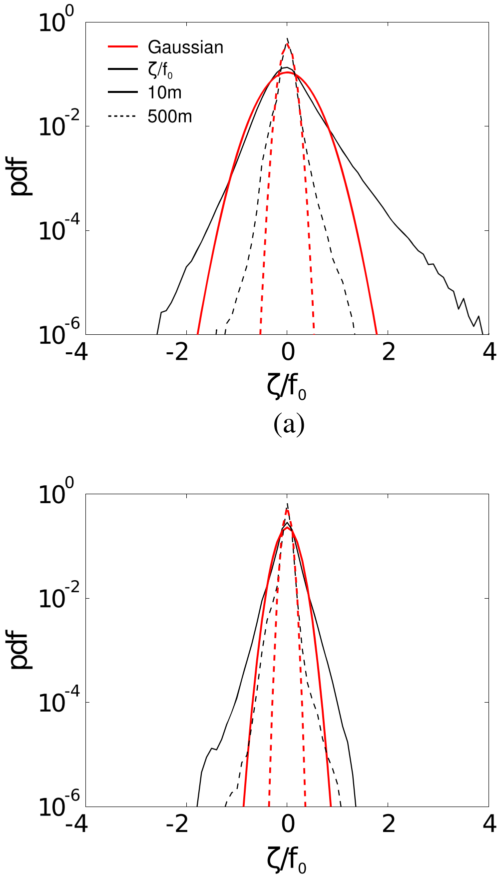

(a)

(b)

Fig. 13 PDF of relative vorticity for winter season, HR (*top panel*) and LR (*bottom panel*), normalized over f_0. The *solid lines* are for PDFs at a 10-m depth and the *dashed line* for PDFs computed at a 500-m depth. The *red lines* represent the PDF of the normal distribution computed with the same standard deviation as the 10-m depth PDF and with zero mean

development of strong tails especially in the positive side. The positive asymmetry is consistent with flows generating in the presence of frontogenesis and MLI (Hoskins 1982; Hoskins et al. 1978; Rudnick 2001; Thomas and Lee 2005; Klein et al. 2008).

4.4 Okubo–Weiss parameter

We conclude the flow diagnostics computing the Okubo–Weiss parameter (OW). OW is a metric used to identify elliptic (vorticity-dominated) and hyperbolic (strain-dominated) regions, which has been often applied to 2D or quasi-geostrophic quasi-non-divergent flows (Weiss 1991; Okubo 1970). For the general case of a non-null horizontal divergence field (Petersen et al. 2006; Zavalasanson and Sheinbaum 2008), OW can be written as follows:

$$\begin{aligned}\mathrm{OW} &= S^2 - \zeta^2 \\ &= \delta^2 + 4\left(\frac{\partial u}{\partial y}\frac{\partial v}{\partial x} - \frac{\partial u}{\partial x}\frac{\partial v}{\partial y}\right) = \delta^2 - 4\,\mathrm{Det}(\nabla_h \mathbf{u}). \quad (9)\end{aligned}$$

where $\mathbf{u} = (u, v)$, $S^2 = S_1^2 + S_2^2 = (\partial u/\partial x - \partial v/\partial y)^2 + (\partial v/\partial x + \partial u/\partial y)^2$, $\zeta^2 = (\partial v/\partial x - \partial u/\partial y)^2$ is the square of the relative vorticity, $\delta = \nabla_h \cdot \mathbf{u} = \partial u/\partial x + \partial v/\partial y$ is the horizontal flow divergence, and $\mathrm{Det}(\nabla_h \mathbf{u})$ is the determinant of the velocity tensor gradient $\nabla_h \mathbf{u}$. Notice that S^2 exactly corresponds to the determinant of the horizontal strain rate for divergence free fields, while in divergent flows, S^2 also includes a divergence component (Provenzale 1999).

Figure 14 shows two typical snapshots of OW computed in winter and summer in the mixed layer for HR and LR. The S^2 term appears dominant in winter HR (positive OW),

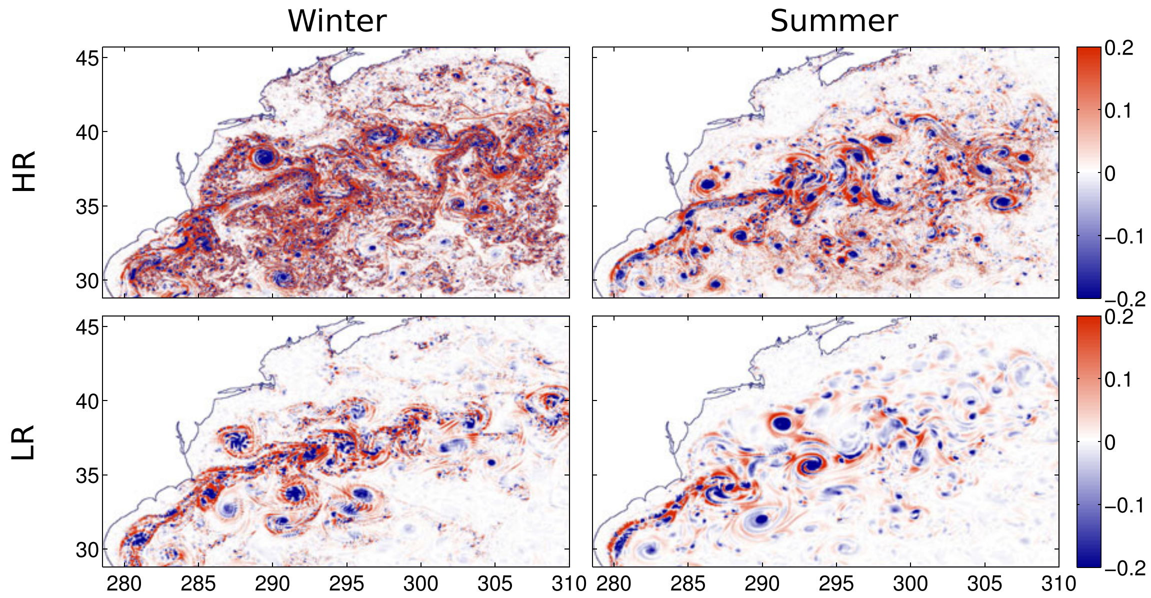

Fig. 14 Okubo–Weiss parameter normalized by f_0^2 computed at the surface (5 m) for winter (*left column*), summer (*right column*), HR (*top row*), and LR (*bottom row*)

therefore indicating a direct connection with the submesoscale field. As discussed above, S^2 is a signature not only of strain but also of divergence, which appears to be strongly increased in winter likely because of frontogenesis and MLI.

Seasonality of OW is quantitatively shown by the time series in Fig. 15, obtained by computing OW, S^2, ζ^2, δ^2 integrating over region A at a 5-m depth. Differently from what is expected for a divergent free closed flow (Petersen et al. 2006), OW appears to be significantly different from zero especially for HR during winter, showing mostly positive values.

In order to better understand the behavior of the integrated OW, consider the following form of Eq. 9 in terms of the gradient (Zavalasanson and Sheinbaum 2008),

$$\mathrm{OW} = \delta^2 - 2\nabla_h \cdot (\mathbf{u}\,\delta) + 2\nabla_h(\mathbf{u} \cdot \nabla_h \mathbf{u}). \tag{10}$$

When Eq. 10 is integrated over a domain, the last two terms on the right-hand side can be rewritten as closed path integrals which depend on the boundary conditions,

$$\int_A \mathrm{OW}\, d\mathbf{A} = \int_A \delta^2\, d\mathbf{A} \overbrace{- 2\oint \mathbf{u}\,\delta d\mathbf{r} + 2\oint \mathbf{u} \cdot \nabla_h \mathbf{u}\, d\mathbf{r}}^{\text{Boundary Terms}}. \tag{11}$$

Equation 11 implies that OW is zero when the flow is nondivergent and computed in a closed domain with no-slip boundary conditions. In our case, both components of the r.h.s. are expected to be different from zero, therefore contributing to a net value of OW. The δ^2 component (shown in Fig. 15 in blue) is indeed of the same order as the total OW (shown in red), suggesting that it is a predominant factor. The difference between OW and δ^2 is likely to be due to the boundary condition effects.

Ultimately, the time series of OW and its components shows that, while LR is essentially 2D and geostrophic, HR experiences a seasonal transition from a quasi-2D divergence-free regime during the summer to a more three-dimensional regime during the winter season, which is another indication of deviation from geostrophic balance. This transition is on top of an increased hyperbolicity of the flow field during the winter season as many filaments and fronts develop in the proximity of large and mesoscale features.

5 Role of stratification and mixed layer depth on submesoscale seasonality

In the previous sections, we have shown that submesoscale features are mostly present during winter and in the mixed layer. Here, we investigate the main environmental parameters controlling the observed seasonality.

We build on the results of a number of previous works, mostly based on idealized numerical experiments, that investigated the relationship between the development of MLI and consequent occurrence of SM features in relation to ambient parameters (Boccaletti et al. 2007; Klein et al. 2008; Lapeyre et al. 2006; Thomas et al. 2008; Molemaker et al. 2010; Lévy et al. 2001; Özgökmen et al. 2011; Fox-Kemper et al. 2008; Fox-Kemper and Ferrari 2008; Capet et al. 2008a; Badin et al. 2011). In

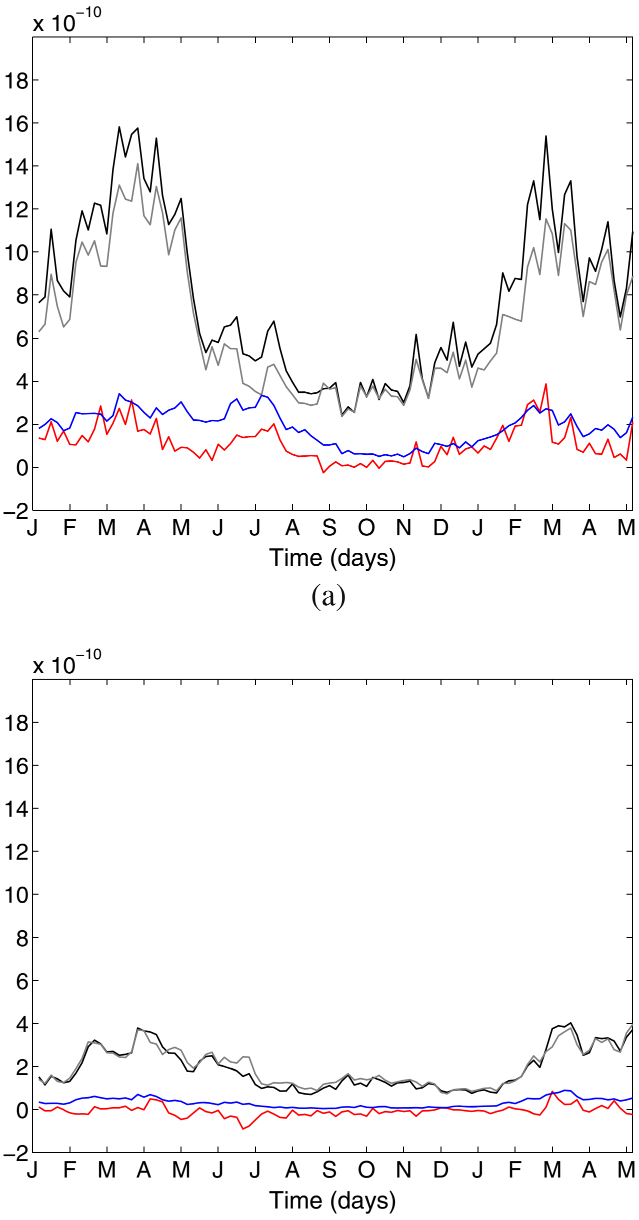

(a)

(b)

Fig. 15 Temporal evolution of the components of the Okubo–Weiss parameter (per square second, from Eq. 9) integrated over region A at a 5-m depth for **a** HR and **b** LR: OW parameter (*red line*), S^2 (strain rate, *black line*), ζ^2 (relative vorticity squared, *gray line*), and δ^2 (divergence squared, *blue line*)

particular, we focus on the works by (Boccaletti et al. 2007; Fox-Kemper et al. 2008; Fox-Kemper and Ferrari 2008) who investigated the dependence of MLI from the parameters of several ideal flows, including a channel with mesoscale eddies and an isolated mixed layer front, varying in particular the main stratification and lateral density gradients.

MLIs are expected to be relevant in terms of transfer of buoyancy fluxes. The buoyancy equation for the total (meso and submesoscale) buoyancy can be written as follows:

$$\frac{\partial}{\partial t}\left(\bar{b}+b'\right)+\nabla\cdot\left[\left(\bar{\mathbf{u}}+\mathbf{u}'\right)\cdot\left(\bar{b}+b'\right)\right]=-\mathcal{F}, \qquad (12)$$

where $\mathbf{u}$ is the three-dimensional velocity; primes indicate the SM component; and $\mathcal{F}$ indicates the solar and diffusive fluxes. As reviewed in Section 3.2, the SM-integrated vertical buoyancy flux term, $w'b'$, is expected to be significant in the presence of mixed layer fronts when MLIs develop and is related to a transfer between APE stored in the fronts and EKE, leading to slumping of the fronts and restratification of the mixed layer. (Fox-Kemper et al. 2008) proposed a simple parameterization for this term written as an overturning stream function with a given scaling and vertical structure. The scaling for the total APE conversion can be written as follows (Capet et al. 2008a):

$$\mathrm{PK}=\left\langle w'b'\right\rangle_{xyz}\propto\left\langle|\nabla\bar{b}|\right\rangle^{2}_{xyz}\cdot\left\langle\mathrm{MLD}\right\rangle^{2}_{xy}, \qquad (13)$$

where $\langle.\rangle_{xy}$ indicates horizontal averaging over region A, and $\langle.\rangle_{xyz}$ volume averaging over region A and over MLD. Equation 13 is valid under the assumption that the flow field is dominated by advection, as is the case of SM regime, and that horizontal velocities scale according to the thermal wind relationship. The complete parameterization by (Fox-Kemper et al. 2008) has been tested using idealized model results (Fox-Kemper and Ferrari 2008), while the validity of the integrated scaling in Eq. 13 has been tested by (Capet et al. 2008a) using a realistic model of the Argentinian shelf.

Conceptually, Eq. 13 assumes that there are two main parameters influencing MLIs and their effects: the presence of horizontal density gradients, i.e., fronts, in the mixed layer, and the depth of the mixed layer, MLD. Shallow mixed layer and strong surface stratification inhibit the formation of vertical recirculations along the flanks of fronts, while in the presence of deep mixed layer and low surface stratification, the cells are enhanced, and a great reservoir of APE is available for MLIs giving rise to significant SM features.

In the following, we aim at quantitatively testing the integrated scaling (13). The GS region is expected to be different from the idealized settings analyzed before and also from the coastal or upwelling-dominated areas considered by Capet et al. (2008a, d), insofar it is influenced by very strong mesoscale nonlinearity and strain. In the next subsection, we provide an analysis of the stratification and MLD seasonality in our GS model.

5.1 Seasonality of surface stratification and MLD

The seasonal variation of the upper ocean stratification is first qualitatively shown in terms of snapshots of vertical sections of potential density and monthly mean profiles (Fig. 16). During the winter season, a weakly stratified and deep mixed layer is established. This allows meso- and large-scale features to outcrop at the surface and generate deep fronts in the mixed layer. During the summer season on the other hand, a strongly stratified and warm mixed layer is established, which counteracts the outcropping of features from below the mixed layer. Strong density gradients are generated during spring at the base of the mixed layer when the relatively warm mixed layer interacts with cold mesoscale features generating in the thermocline. During the summer season (August), density gradients are high only at the very base of the mixed layer, and the stratification becomes strong enough to inhibit mesoscale features from reaching the surface.

Seasonality of surface stratification is reflected on the MLD. Figure 16 shows vertical density profiles and MLD averaged over a 1-month period, confirming the presence of a deep mixed layer during the winter season and a shallow mixed layer during the summer season.

The seasonal cycle of MLD is shown in Fig. 17a for both HR and LR, indicating that the mixed layer depth reaches approximately 200 m during winter, while it quickly becomes shallow in the spring, starting in April, reaching a minimum of less than 10 m by June. The difference in HR and LR MLD values reaches a maximum of the order of 50 m during the winter season, with the LR MLD being deeper than the HR.

Since the only difference between the two simulations is resolution, with consequent occurrence of SM features in

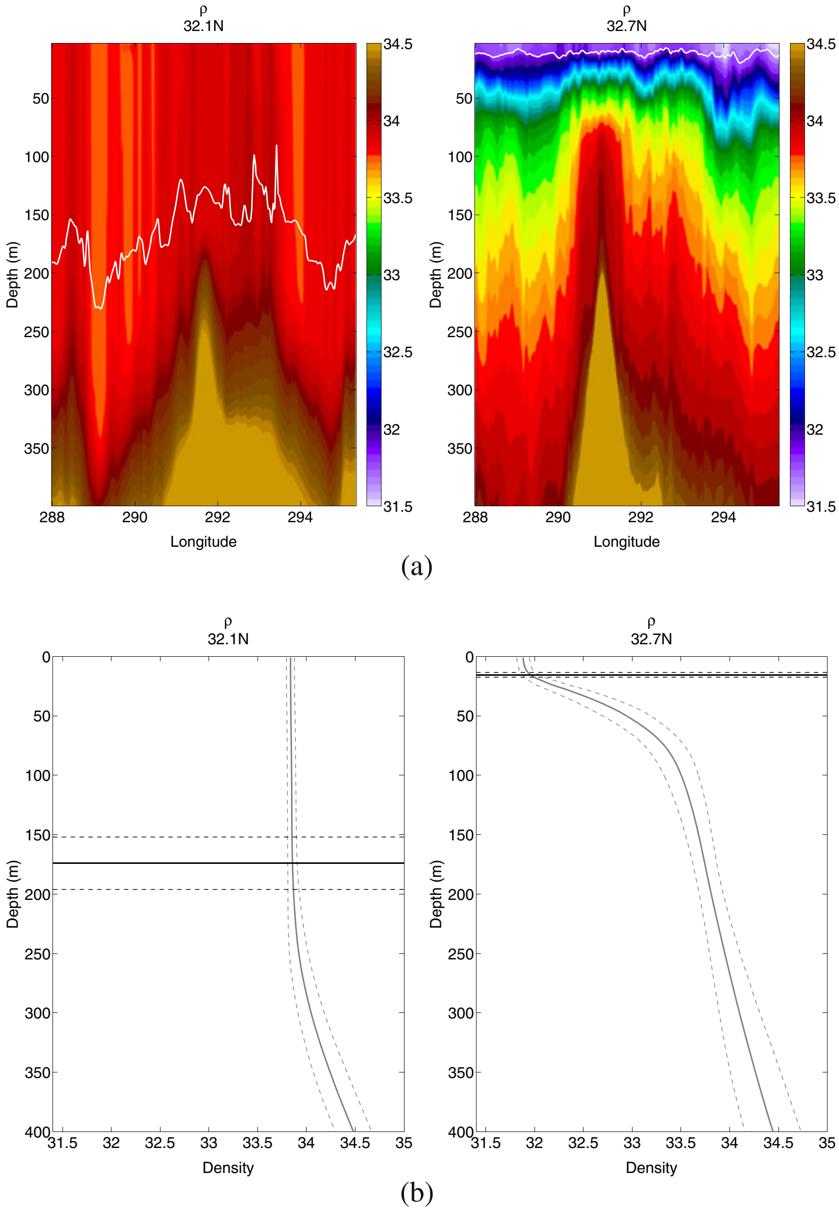

(a)

(b)

Fig. 16 Density (σ_2) sections showing the vertical stratification for the winter (*left panels*) and summer (*right panels*) season in the HR simulation. In the *top panels*, daily snapshots are shown, while averages for the same sections over 1 month are shown in the *lower panels* (*dashed lines* are the mean values plus or minus the standard deviation). Mixed layer depth is represented by a *white line* in the *top panels* and *black line* in the *lower panels*

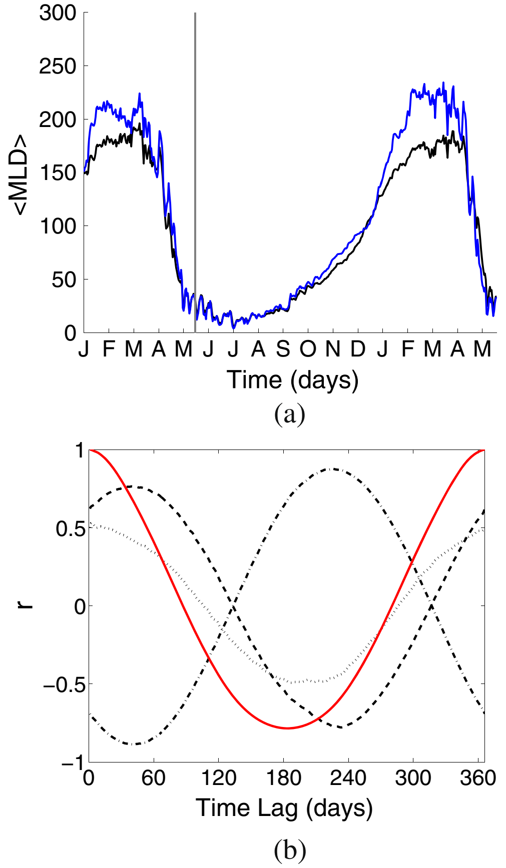

(a)

(b)

Fig. 17 **a** Temporal variability of the mixed layer depth (in meter) averaged over region A (*black line*, HR; *blue line*, LR). **b** The correlation in time between surface forcings (f_T, *dashed line*; f_S, *dashed-dotted line*; and u^*, *dotted line*), and mixed layer depth is shown for the last 365 days of the simulation. *Red line* in **b** represents the mixed layer autocorrelation function. The *gray line* in **a** represents the begin of the portion of the time series that has been used to compute $r[t]$

HR, this is a clear indication that, indeed, SM restratification tends to compact the isopycnals leading to a significant change in the winter MLD. We notice that such an effect is not observed in the simulations of Capet et al. (2008b) in the California Current, where the HR mixed layer does not become shallower, even though MLI flux divergence is clearly present. Capet et al. (2008b) argue that this is due to the fact that the increasing vertical flux is counterbalanced by an increase in vertical mixing, which tends to destratify the flow. They also suggest that this effect might be overestimated in their simulations because of their constant forcing. In our simulations, wind synoptic scales, seasonal flux variations, and high variability in mesoscale fronts are likely to sustain MLI effects over boundary layer turbulence. In particular, wind has been shown to be able to intensify surface density fronts and to affect the magnitude of the across-front ageostrophic circulation (Thomas and Lee 2005; Capet et al. 2008c; Cardona and Bracco 2012). Nevertheless, we did not observe the same strong correlation between the magnitude of ω and down-front winds observed, for example, in the California Current by Capet et al. (2008c). This difference might be due to the presence of a strong mesoscale field in the GS region which ultimately controls the orientation and intensity of ML fronts.

The MLD seasonality is clearly linked to the atmospheric forcings. Both HR and LR simulations are forced with a realistic perpetual year forcing, and seasonality can be quantified in terms of mean surface fluxes of heat (f_T [in watt per square meter]) and salinity (f_S [$10^{-3}\,\mathrm{kg\,m^{-2}\,s^{-1}}$]) and a mechanical forcing represented by wind speed (u^* [in meter per second]). Details on how these quantities are computed in HYCOM and their seasonal cycles are shown in the Appendix.

In order to quantify the degree of the correlation between MLD and the atmospheric forcings, we computed the cross-correlation (defined as a sliding cross product by the $\star$) between the time series of each forcing and mixed layer depth:

$$r[t] = (f_{T,S,u^*} \star \mathrm{MLD})[t] \;\equiv \sum_{m=0}^{365} f_{T,S,u^*}[m]\, \mathrm{MLD}[m+t], \tag{14}$$

Results are shown in Fig. 17b, where the cross-correlation $r[t]$ is computed for f_T (dashed line), f_S (dashed-dotted line), and u^* (dotted line). The red solid line represents the autocorrelation curve computed as the cross-correlation of MLD with respect to itself and represents the ideal cross-correlation. Cross-correlation is computed by assuming the last 365 days of MLD and forcings.

The time series for MLD shows a good correlation (with maximum correlation of $r \sim 0.8$) with both buoyancy fluxes (dashed and dashed-dotted lines), while it is slightly lower for the wind (maximum correlation of $r \sim 0.6$). Time series of surface fluxes and mixed layer depth are shifted in time due to the fact that the maximum flux corresponds to the maximum time derivative of the ocean response. As a result, the maximum of mixed layer depth occurs $\sim$ 60 days after the minimum of f_T and the maximum of f_S. The time lag is nearly zero in the case of the mechanical forcing (u^*). In summary, the seasonality of MLD is forced by the fluxes of buoyancy and wind speed.

5.2 Dependence of MLIs on MLD

Here, we quantitatively test whether the scaling in Eq. 13 is valid for our realistic GS simulation similarly to what has been done by Capet et al. (2008a) for the Argentinian shelf simulation. The various terms in Eq. 13 have been computed for the HR simulation, and the corresponding time series are shown in Fig. 18. Sensitivity tests have been done for

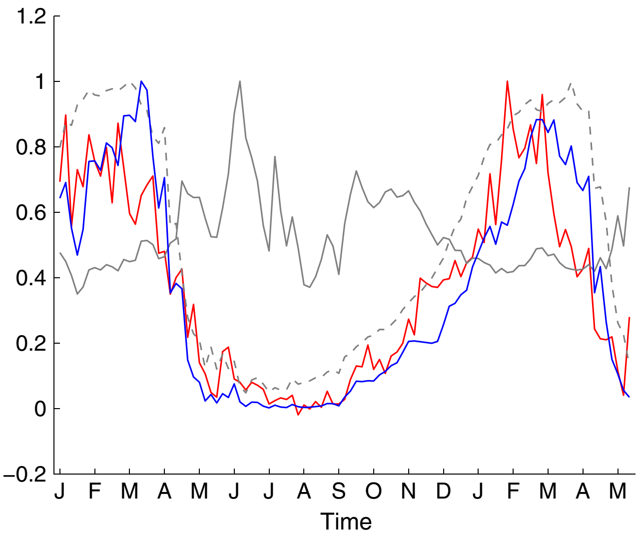

Fig. 18 Time series of the terms in Eq. 13 for HR. $\langle w'b'\rangle_{xyz}$ in *red*, $\langle|\nabla\bar{b}|\rangle^2_{xyz}\cdot\langle\mathrm{MLD}\rangle^2_{xy}$ in *blue*, $\langle|\nabla\bar{b}|\rangle_{xyz}$ in *solid gray*, and $\langle\mathrm{MLD}\rangle_{xy}$ in *dashed gray*. All curves are normalized over the maximum value of each time series

different values of the sine filter wave length showing some sensitivity to the values of λ. In particular, choosing a value of $\lambda = 40$ km gives values of $w'b'$ too small during the spring and fall seasons.

The overall agreement between the two sides of Eq. 13 (blue and red lines) is satisfactory, indicating that the scaling holds, similarly to what was found by Capet et al. (2008a). It is interesting to notice though that the horizontal gradient term $\langle|\nabla\bar{b}|\rangle_{xyz}$ shows a significantly different behavior with respect to MLD. While MLD is maximum in winter and very shallow from May to September, the horizontal gradient term has a less well-defined and more complex structure. A minimum can be seen around August and September, when stratification is the strongest and effectively isolates the mixed layer from the internal mesoscale structure, but during spring and autumn, there are clear peaks. The term has a very high variability over monthly scales, likely due to oscillations of the large-scale Gulf Stream fronts and formation and advection of mesoscale eddies and rings.

From the physical point of view, the results indicate that the limiting and controlling factor in SM formation in the GS region is indirectly MLD. Horizontal gradients and surface fronts are present in this area almost during the whole year, but the stratification inhibits the formation of deep recirculating cells and significant MLIs. This is different from what was found by Capet et al. (2008a) in the Argentinian shelf where lateral gradients have a maximum approximately in phase with MLD, and they are both related to atmospheric forcing. Here, atmospheric forcings are still the main controlling factor, but only through the control of MLD. Horizontal gradients are provided by the vigorous mesoscale field that is present during the whole annual cycle, except for a brief period at the end of summer when stratification shuts them down in the mixed layer.

6 Conclusions

In this paper, results from a realistic HR simulation of the region of the Gulf Stream recirculation are presented, with the goal of investigating SM processes in the mixed layer and their seasonality. Results show that during the winter season, deep vertical recirculations are observed to develop associated to fronts outcropping from mesoscale eddies and rings into the mixed layer. MLIs are generated at these fronts, leading to the formation of a vigorous submesoscale field. During summer, on the other hand, the occurrence of vertical recirculations and MLIs appear damped, and the SM field is much weaker.

The characteristics of the mixed layer flow and the occurrence of SM features have been quantitatively characterized in statistical terms. SM features, with scales of the order of the mixed layer Rossby radius, appear characterized during winter by a clear deviation from geostrophy, high Rossby number, with prevalently positive vorticity, and significant divergence.

Results of the HR simulations are compared to results from the LR simulation where submesoscale features are not resolved. In the LR results, seasonality of the mixed layer flow is much reduced, and the field is dominated by mesoscale during the whole year, with relatively small deviations from geostrophy and a quasi-2D behavior.

We then investigate the main environmental parameters that control the observed SM seasonality, building on previous results from idealized numerical studies and realistic simulation (Özgökmen et al. 2011; Badin et al. 2011; Boccaletti et al. 2007; Capet et al. 2008a, b, c, d; Fox-Kemper and Ferrari 2008; Fox-Kemper et al. 2008; Molemaker et al. 2010).

The flow field is filtered to separate meso and larger scales from SM. Isolating the SM anomalies allows to apply the scaling of the total SM vertical buoyancy flux in the mixed layer, PK, proposed by (Fox-Kemper et al. 2008). PK quantifies the APE release associated to MLIs and can be considered as a measure of the presence of SM features in the field. The scaling by Fox-Kemper et al. (2008) and Capet et al. (2008a) links PK with the presence of mesoscale surface lateral gradients in the mixed layer, indicative of surface fronts, and with the magnitude of mixed layer depth MLD. Direct testing with our results shows that the scaling is appropriate, following the same seasonal variations as the observed PK. The governing factor appears to be MLD, while horizontal gradients appear present during the whole year because of the presence of mesoscale eddies and rings. This result is different from what was obtained by Capet et al. (2008a) in the Argentinian Shelf, where the seasonality of both horizontal gradients and MLD contributes to the scaling, and both are induced by atmospheric forcing. In our case, atmospheric fluxes and wind forcing are still the cause of SM occurrence, but mostly through their action on MLD. While surface fronts are always available, the deep MLD during winter provides a much greater reservoir of APE, which allows MLIs to develop a vigorous SM field.

The importance of MLIs on the large scales is suggested by the comparison between the mixed layer in HR and LR. The mixed layer in HR is shallower than in LR of approximately 50 m, i.e., of a significant $\sim$ 25 %, suggesting that the restratification induced by SM is the cause of mixed layer shoaling.

We notice that this finding is different from what was shown in Capet et al. (2008b, c, d) in the California upwelling simulations, where MLD did not change significantly between HR and LR simulations. As suggested by Capet et al. (2008b), this is likely due to their numerical setting characterized by constant forcing, which allows destratifying effects by vertical mixing to counteract the stratifying effects of MLIs. In our simulations, instead, atmospheric variability and mesoscale-induced frontal variability appear to maintain MLI activity and their stratifying effects.

Overall the results provide a first picture of SM dynamics in the complex GS region, characterized by strong nonlinear mesoscale interactions. One of the main results is that MLIs appear to be one of the main mechanisms leading to a vigorous winter SM field, mostly due to deepening of the mixed layer and increased APE reservoir. MLI structure and their scaling appear well captured by the parametrization proposed by Fox-Kemper et al. (2008), indicating that the relationship is appropriate even in this complex and mesoscale-dominated area.

A number of future avenues can be foreseen. While we have concentrated here mostly on the effects of MLIs, a more in-depth analysis of frontogenesis mechanisms is expected to shed further light on the SM dynamics of the area. Also, there are a number of aspects that can be further refined with dedicated numerical experiments at higher horizontal and vertical resolution, especially during the summer season when the very shallow mixed layer induces a very small SM Rossby number.

Acknowledgments We greatly appreciate the support of the National Science Foundation via grant OCE-0850714 and grant OCE-0850690 the Office of Naval Research via grant N00014-09-1-0267 and DMS-1025323. This research was also supported by the ONR grant N00014-11-1-0087 under the Multidisciplinary University Research Initiative on Dynamical Systems Theory Ocean 3D + 1. Discussions with ONR Lateral Mixing Group were most appreciated. We thank the computing center of the University of Miami (http://ccs.miami.edu/hpc/) Yeon Chang, Gustavo Mastrorocco Marques and the ISMAR-CNR in Lerici (SP, Italy) for the support.

Appendix

Surface fluxes parametrization

Thermal energy flux into the ocean (f_T [in watt per square meter]) is computed by HYCOM from the balance between incident radiation and emitted ocean radiation ($\mathcal{R}$), the latent heat transfer ($\mathcal{H}$), and the sensible heat transfer due to evaporation (ϵ),

$$f_T = \mathcal{R} - \epsilon - \mathcal{H}. \tag{15}$$

$\mathcal{R}$ (in watt per square meter), the net solar radiation (as well as its short and long wave components), is positive into the ocean and is provided as forcing. The surface radiation budget also includes a black body radiation correction flux, proportional to the difference between the surface temperature and the air temperature of the data used for the forcing (ERA40).

Latent heat transfer due to evaporation, ϵ, is computed from

$$\epsilon = L_{\mathrm{E}} \rho_{\mathrm{a}} u^* C_{\mathrm{L}} (T_s - T_w), \tag{16}$$

where L_{E} is the latent heat of evaporation coefficient ($2.47 \cdot 10^6$ j kg^{-1}); ρ_{a} is the air density computed from air temperature; u^* is the 10-m wind speed; C_{L} is the latent heat flux coefficient computed from a polynomial expression, function of stability, and temperature difference between atmosphere and ocean (Kara et al. 2000; Fairall et al. 2003); and T_s and T_w are, respectively, the saturation mixing ratio (from a polynomial expression, function of surface temperature) and water vapor mixing ratio which is provided as part of the (ERA40) forcing.

The last term in the expression of f_T is the sensible heat transfer, $\mathcal{H}$, obtained from

$$\mathcal{H} = C_{P_{\mathrm{air}}} \rho_a C_{\mathrm{S}} u^* (T_{\mathrm{sur}} - T_{\mathrm{atm}}), \tag{17}$$

where $C_{P_{\mathrm{air}}}$ is the specific heat of the air at constant pressure (in joule per kilogram per degree); C_{S} is the sensible heat flux coefficient computed by Kara et al. (2000) as $0.9554 \cdot C_{\mathrm{L}}$; T_{sur} is the model sea surface temperature; and T_{atm} is the air temperature.

The salinity flux into the ocean, f_S ($[10^{-3}$ kg m^{-2} s$^{-1}]$), is quantified in the model as follows:

$$f_S = (E - P) \cdot (S \cdot 10^3), \tag{18}$$

where E the is evaporation rate

$$E = \epsilon \cdot 10^{-3}/L_{\mathrm{E}}, \tag{19}$$

P is precipitation (given as a forcing), and S is the salinity at the surface. In addition, a relaxation of sea surface salinity to climatology is included.

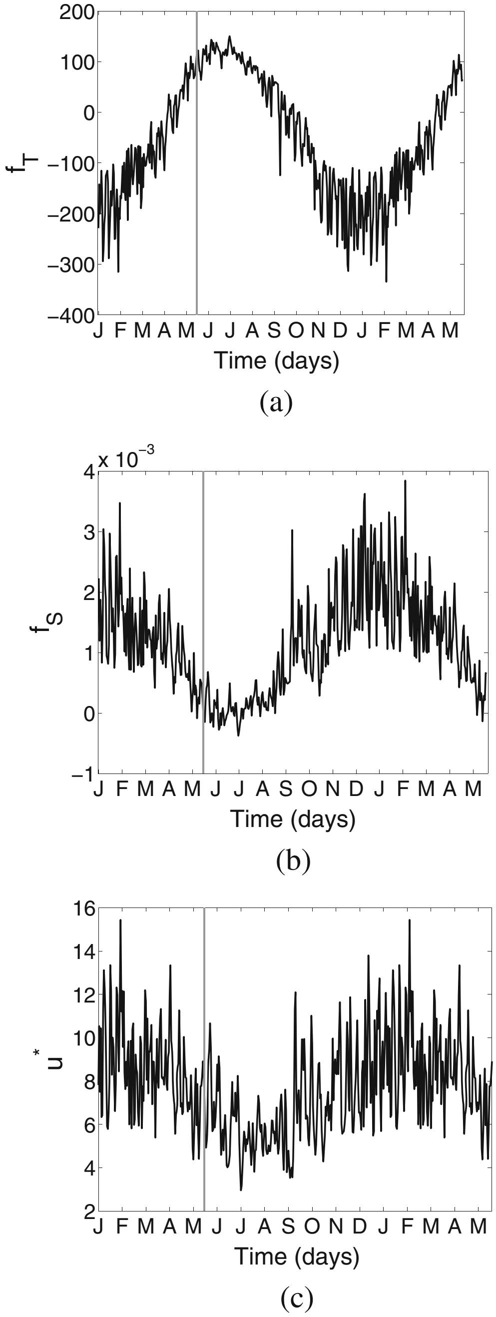

(a)

(b)

(c)

Fig. 19 Temporal variability of the bulk fluxes of **a** heat (in watt per square meter), **b** salinity $\left[10^{-3}\,\mathrm{kg\,m^{-2}\,s^{-1}}\right]$, and **c** wind speed (in meter per second) averaged over region A. The *gray line* represents the first point of the time series considered

In Fig. 19a, the seasonal variability of f_T averaged over region A is shown. Values are negative during the winter season and positive during the summer, representing a heat flux from the ocean to atmosphere during the winter and a net heat gain of the ocean during the summer. Analogously, in Fig. 19b, the spatially averaged values of f_S in time are shown with maxima and minima shifted of approximately half period with respect to f_T. Average values of f_S are always positive in region A, evaporation being larger than precipitation; f_S contributes to the mixed layer being saltier during winter and fresher during summer.

During the winter season, negative values of f_T act to increase density reducing the ocean temperature, while positive values of f_S contribute to increase salinity and thus density. During the summer season on the other side, f_S is nearly zero due to weak evaporation, and density is driven only by f_T which is positive into the ocean. Buoyancy fluxes ultimately affect MLD by stratifying the upper ocean during summer and destratifying the mixed layer in winter.

Wind speed (u^*) enters in the equations as a factor in the formulation of sensible heat and evaporation. The wind speed seasonal cycle (Fig. 19c) shows a maximum in winter and a cycle similar to f_S. Wind speed enters in the formulation of both f_s and f_T favoring the latent heat transfer due to evaporation (16) and thus producing a loss of heat (15) and a gain of salinity (19) at the surface.

References

Auer SJ (1987) Five-year climatological survey of the Gulf Stream system and its associated rings. J Geophys Res 92:11709

Badin G, Tandon A, Mahadevan A (2011) Lateral mixing in the pycnocline by baroclinic mixed layer eddies. J Phys Oceanogr 41:2080–2101

Bishop C (1993) On the behaviour of baroclinic waves undergoing horizontal deformation. II. Error-bound amplification and Rossby wave diagnostics. Q J R Meteorol Soc 510:241–267

Bleck R (2002) An oceanic general circulation model framed in hybrid isopycnic-Cartesian coordinates. Ocean Model 4:55–88

Boccaletti G, Ferrari R, Fox-Kemper B (2007) Mixed layer instabilities and restratification. J Phys Oceanogr 37:2228–2250

Capet X, Campos EJ, Paiva aM (2008a) Submesoscale activity over the Argentinian shelf. Geophys Res Lett 35:2–6

Capet X, McWilliams JC, Molemaker MJ, Shchepetkin AF (2008b) Mesoscale to submesoscale transition in the California current system. Part I: flow structure, eddy flux, and observational tests. J Phys Oceanogr 38:29–43

Capet X, McWilliams JC, Molemaker MJ, Shchepetkin AF (2008c) Mesoscale to submesoscale transition in the California current system. Part II: frontal processes. J Phys Oceanogr 38:44–64

Capet X, McWilliams JC, Molemaker MJ, Shchepetkin AF (2008d) Mesoscale to submesoscale transition in the California current system. Part III: energy balance and flux. J Phys Oceanogr 38:2256–2269

Cardona Y, Bracco A (2012) Enhanced vertical mixing within mesoscale eddies due to high frequency winds in the South China Sea. Ocean Model 42:1–15

Chang YS, Garraffo ZD, Peters H, Özgökmen TM (2009) Pathways of Nordic overflows from climate model scale and eddy resolving simulations. Ocean Model 29:66–84

Chassignet E, Garraffo Z (2001) Viscosity parameterization and the Gulf Stream separation. In: Proceedings 'Aha Huliko'a Hawaiian winter workshop. University of Hawaii pp 15–19

Chassignet E, Smith TL, Halliwell GR, Bleck R (2003) North Atlantic simulations with the Hybrid Coordinate Ocean Model (HYCOM): impact of the vertical coordinate choice, reference pressure, and thermobaricity. J Phys Oceanogr 33:2504–2526

Chassignet E, Hurlburt H, Smedstad O, Halliwell G, Hogan P, Wallcraft A, Bleck R (2006) Ocean prediction with the hybrid coordinate ocean model (HYCOM). Ocean weather forecasting, pp 413–426

Chassignet E, Hurlburt H, Metzger E, Smedstad O, Cummings J, Halliwell G, Bleck R, Baraille R, Wallcraft A, Lozano C, Tolman H, Srinivasan A, Hankin S, Cornillon P, Weisberg R, Barth RHA, Werner F, Wilkin J (2009) US GODAE: global ocean prediction with the HYbrid Coordinate Ocean Model (HYCOM). Oceanography 22:64–75

Chelton D, Schlax M, El Naggar K, Siwertz N (2010) Geographical variability of the first baroclinic Rossby radius of deformation. J Phys Oceanogr 28:433–460

Clarke R, Hill H, Reiniger R, Warren B (1980) Current system south and east of the Grand Banks of Newfoundland. J Phys Oceanogr 10:25–65

D'Asaro E, Lee C, Rainville L, Harcourt R, Thomas L (2011) Enhanced turbulence and energy dissipation at ocean fronts, vol. 332. Science, New York, pp 318–322

Ducet N, Le Traon PY, Reverdin G (2000) Global high-resolution mapping of ocean circulation from TOPEX/Poseidon and ERS-1 and -2. J Geophys Res 105:19477

Eldevik T (2002) Spiral eddies. J Phys Oceanogr 32:851–869

Fairall C, Bradley E, Hare J, Grachev A, Edson J (2003) Bulk parameterization of air-sea fluxes: updates and verification for the COARE algorithm. Am Meteorol Soc 16:571–592

Ferrari R, Rudnick D (2000) Thermohaline variability in the upper ocean. J Geophys Res 105:16857–16883

Flament P, Armi L, Washburn L (1985) The evolving structure of an upwelling filament. J Geophys Res 90:11765–11778

Fox-Kemper B, Ferrari R (2008) Parameterization of mixed layer eddies. Part II: prognosis and impact. J Phys Oceanogr 38:1166–1179

Fox-Kemper B, Ferrari R, Hallberg R (2008) Parameterization of mixed layer eddies. Part I: theory and diagnosis. J Phys Oceanogr 38:1145–1165

Fratantoni DM (2001) North Atlantic surface circulation during the 1990's observed with satellite-tracked drifters. J Geophys Res Oceans 106:22067–22093

Garraffo Z, Mariano A, Griffa A, Veneziani C, Chassignet EP (2001) Lagrangian data in a high-resolution numerical simulation of the North Atlantic: I. Comparison with in situ drifter data. J Mar Syst 29:157–176

Giordani H, Caniaux G (2001) Sensitivity of cyclogenesis to sea surface temperature in the Northwestern Atlantic. Mon Weather Rev 129:1273–1295

Giordani H, Planton S (2000) Modeling and analysis of ageostrophic circulation over the Azores oceanic front during the SEMAPHORE experiment. Mon Weather Rev 128:2270–2287

Haine TWN, Marshall J (1998) Gravitational, symmetric, and baroclinic instability of the ocean mixed layer. J Phys Oceanogr 28:634–658

Halliwell G (2004) Evaluation of vertical coordinate and vertical mixing algorithms in the HYbrid-Coordinate Ocean Model (HYCOM). Ocean Model 7:285–322

Haza A, Özgökmen T, Griffa A, Garraffo ZD, Piterbarg L (2012) Parameterization of particle transport at submesoscales in the Gulf Stream region using Lagrangian subgridscale models. Ocean Model 42:31–49

Hogg NG (1992) On the transport of the gulf stream between Cape Hatteras and the Grand Banks. Deep Sea Res Part I Oceanogr Res Pap 39:1231–1246

Hoskins B (1982) The mathematical theory of frontogenesis. Annu Rev Fluid Mech 14:131–151

Hoskins BJ, Bretherton FP (1972) Atmospheric frontogenesis models: mathematical formulation and solution. J Atmos Sci 29:11–37

Hoskins B, Draghici I, Davies H (1978) A new look at the ω-equation. Q J R Meteorol Soc 104:31–38

Johns W, Shay T, Bane J, Watts D (1995) Gulf stream structure, transport, and recirculation near 68 W. J Geophys Res 100:817–838

Kara A, Rochford P, Hurlburt HE (2000) Efficient and accurate bulk parameterizations of air sea fluxes for use in general circulation models. J Atmos Ocean Technol 17:1421–1438

Kara AB, Wallcraft AJ, Hurlburt HE (2007) A correction for land contamination of atmospheric variables near land–sea boundaries. J Phys Oceanogr 37:803–818

Klein P, Lapeyre G (2009) The oceanic vertical pump induced by mesoscale and submesoscale turbulence. Annu Rev Mar Sci 1:351–375

Klein P, Hua B, Lapeyre G, Capet X, Le Gentil S, Sasaki H (2008) Upper ocean turbulence from high-resolution 3D simulations. J Phys Oceanogr 38:1748–1763

Kolmogorov A (1941) Dissipation of energy in the locally isotropic turbulence Proceedings mathematical and physical sciences. The Royal Society, London

Koszalka I, LaCasce JH, Orvik KA (2009) Relative dispersion in the Nordic Seas. J Mar Res 67:411–433

Lapeyre G, Klein P, Hua BL (2006) Oceanic restratification forced by surface frontogenesis. J Phys Oceanogr 36:1577

Large W, McWilliams J, Doney S (1994) Oceanic vertical mixing: a review and a model with a nonlocal boundary layer parameterization. Rev Geophys 32:363–403

Lévy M, Klein P, Treguier A-M (2001) Impact of sub-mesoscale physics on production and subduction of phytoplankton in an oligotrophic regime. J Mar Res 59:535–565

Lévy M, Iovino D, Resplandy L, Klein P, Madec G, Tréguier A-M, Masson S, Takahashi K (2011) Large-scale impacts of submesoscale dynamics on phytoplankton: local and remote effects. Ocean Model 44:77–93

Lumpkin R, Elipot S (2010) Surface drifter pair spreading in the North Atlantic. J Geophys Res 115:1–20

Lumpkin R, Johnson GC (2013) Global ocean surface velocities from drifters: mean, variance, ENSO response, and seasonal cycle. J Geophys Res Oceans. doi:10.1002/jgrc.20210

Mahadevan A (2006) Modeling vertical motion at ocean fronts: are nonhydrostatic effects relevant at submesoscales? Ocean Model 14:222–240

Mahadevan A, Tandon A (2006) An analysis of mechanisms for submesoscale vertical motion at ocean fronts. Ocean Model 14:241–256

McGillicuddy Jr D, Anderson L, Doney S, Maltrud M (2003) Eddy-driven sources and sinks of nutrients in the upper ocean: results from a 0.1 resolution model of the North Atlantic. Global Biogeochem Cycles 17:1035

McGillicuddy Jr DJ, Anderson LA, Bates NR, Bibby T, Buesseler KO, Carlson CA, Davis CS, Ewart C, Falkowski PG, Goldthwait SA, Hansell DA, Jenkins WJ, Johnson R, Kosnyrev VK, Ledwell JR, Li QP, Siegel DA, Steinberg DK (2007) Eddy/wind interactions stimulate extraordinary mid-ocean plankton blooms, vol. 316. Science, New York, pp 1021–1026

McWilliams J (1985a) A uniformly valid model spanning the regimes of geostrophic and isotropic, stratified turbulence: balanced turbulence. J Atmos Sci 42:1773–1774

McWilliams J (1985b) Submesoscale, coherent vortices in the ocean. Rev Geophys 23:165–182

McWilliams JC (2008) Fluid dynamics at the margin of rotational control. Environ Fluid Mech 8:441–449

McWilliams JC, Colas F, Molemaker MJ (2009a) Cold filamentary intensification and oceanic surface convergence lines. Geophys Res Lett 36:1–5

McWilliams JC, Molemaker MJ, Olafsdottir EI (2009b) Linear fluctuation growth during frontogenesis. J Phys Oceanogr 39:3111–3129

Metzger E, Hurlburt H, Xu X, Shriver J, Gordon A, Sprintall J, Susanto R, van Aken H (2010) Simulated and observed circulation in the Indonesian Seas: 1/12 global HYCOM and the INSTANT observations. Dyn Atmos Oceans 50:275–300

Molemaker MJ, McWilliams JC, Yavneh I (2005) Baroclinic instability and loss of balance. J Phys Oceanogr 35:1505–1517

Molemaker MJ, Mcwilliams JC, Capet X (2010) Balanced and unbalanced routes to dissipation in an equilibrated Eady flow. J Fluid Mech 654:35–63

Muller P, Molemaker MJ, McWilliams J (2005) Routes to dissipation in the ocean: the 2D/3D turbulence conundrum. In: Marine turbulence: theories, observations and models, pp 397–405

Okubo A (1970) Horizontal dispersion of floatable particles in the vicinity of velocity singularities such as convergences. In: Deep sea research and oceanographic abstracts, vol 17. Elsevier, pp 445–454

Özgökmen TM, Fischer PF (2012) CFD application to oceanic mixed layer sampling with Lagrangian platforms. Int J Comput Fluid Dyn 26:337–348

Özgökmen T, Poje A, Fischer P, Haza A (2011) Large eddy simulations of mixed layer instabilities and sampling strategies. Ocean Model 39:311–331

Özgökmen T, Poje A, Fischer P, Childs H, Krishnan H, Garth C, Haza A, Ryan E (2012) On multi-scale dispersion under the influence of surface mixed layer instabilities and deep flows. Ocean Model 56:16–30

Pedlosky J (1987) Geophysical fluid dynamics. Springer study edition. Springer, New York

Petersen MR, Julien K, Weiss JB (2006) Vortex cores, strain cells, and filaments in quasigeostrophic turbulence. Phys Fluids 18: 026601

Pollard R, Regier L (1992) Vorticity and vertical circulation at an ocean front. J Phys Oceanogr 22:609–625

Provenzale A (1999) Transport by coherent barotropic vortices. Annu Rev Fluid Mech 31:55–93

Rudnick DL (2001) On the skewness of vorticity in the upper ocean. Geophys Res Lett 28:2045

Sato O, Rossby T (1995) Seasonal and low frequency variations in dynamic height anomaly and transport of the Gulf Stream. Deep Sea Res Part I Oceanogr Res Pap 42:149–164

Schroeder K, Haza A, Griffa A, Özgökmen TM, Poulain P, Gerin R, Peggion G, Rixen M (2011) Relative dispersion in the Liguro-Provençal basin: from sub-mesoscale to mesoscale. Deep Sea Res Part I Oceanogr Res Pap 58:209–228

Schroeder K, Chiggiato J, Haza A, Griffa A, Özgökmen TM, Zanasca P, Molcard A, Borghini M, Poulain PM, Gerin R, Zambianchi E, Falco P, Trees C (2012) Targeted Lagrangian sampling of submesoscale dispersion at a coastal frontal zone. Geophys Res Lett 39:4–9

Smith R, Maltrud M, Bryan F, Hecht MW (2000) Numerical simulation of the North Atlantic Ocean at 1/10. J Phys Oceanogr 30:1532–1561

Stone P (1966) On non-geostrophic baroclinic stability. J Atmos Sci 23:390–400

Stone P (1970) On non-geostrophic baroclinic stability: part II. J Atmos Sci 27:721–726

Thomas L, Lee C (2005) Intensification of ocean fronts by down-front winds. J Phys Oceanogr 35:1086–1102

Thomas L, Ferrari R (2008) Friction, frontogenesis, and the stratification of the surface mixed layer. J Phys Oceanogr 38:2501–2518

Thomas L, Tandon A, Mahadevan A (2008) Submesoscale processes and dynamics. Ocean Model 177:17–38

Uppala SM, Kllberg PW, Simmons AJ, Andrae U, Bechtold VDC, Fiorino M, Gibson JK, Haseler J, Hernandez A, Kelly GA, Li X, Onogi K, Saarinen S, Sokka N, Allan RP, Andersson E, Arpe K, Balmaseda MA, Beljaars ACM, Berg LVD, Bidlot J, Bormann N, Caires S, Chevallier F, Dethof A, Dragosavac M, Fisher M, Fuentes M, Hagemann S, Hólm E, Hoskins BJ, Isaksen L, Janssen PAEM, Jenne R, Mcnally aP, Mahfouf J-F, Morcrette J-J, Rayner NA, Saunders RW, Simon P, Sterl A, Trenberth KE, Untch A, Vasiljevic D, Viterbo P, Woollen J (2005) The ERA-40 re-analysis. Q J R Meteorol Soc 131:2961–3012

Wallcraft A, Kara A, Barron C (2009) Comparisons of monthly mean 10 m wind speeds from satellites and NWP products over the global ocean. J Geophys Res 114:D16109

Weiss J (1991) The dynamics of enstrophy transfer in two-dimensional hydrodynamics. Physica D Nonlin Phenomena 48:273–294

Zavalasanson L, Sheinbaum J (2008) Elementary properties of the enstrophy and strain fields in confined two-dimensional flows. Eur J Mech B Fluids 27:54–61